remote sensing

MDPI

Article

High-Accuracy Positioning in Urban Environments Using Single-Frequency Multi-GNSS RTK/MEMS-IMU Integration

Tuan Li [1], Hongping Zhang [1,*], Zhouzheng Gao [2,3], Qijin Chen [1] and Xiaoji Niu [1]

[1] GNSS Research Center, Wuhan University, 129 Luoyu Road, Wuhan 430079, China; tuanli@whu.edu.cn (T.L.); chenqijin@whu.edu.cn (Q.C.); xjniu@whu.edu.cn (X.N.)
[2] School of Land Science and Technology, China University of Geosciences, 29 Xueyuan Road, Beijing 100083, China; zhouzhenggao@whu.edu.cn
[3] German Research Centre for Geosciences (GFZ), Telegrafenberg, 14473 Postsdam, Germany
* Correspondence: hpzhang@whu.edu.cn

Received: 18 December 2017; Accepted: 26 January 2018; Published: 30 January 2018

Abstract: The integration of Global Positioning System (GPS) real-time kinematics (RTK) and an inertial navigation system (INS) has been widely used in many applications, such as mobile mapping and autonomous vehicle control. Such applications require high-accuracy position information. However, continuous and reliable high-accuracy positioning is still challenging for GPS/INS integration in urban environments because of the limited satellite visibility, increasing multipath, and frequent signal blockages. Recently, with the rapid deployment of multi-constellation Global Navigation Satellite System (multi-GNSS) and the great advances in low-cost micro-electro-mechanical-system (MEMS) inertial measurement units (IMUs), it is expected that the positioning performance could be improved significantly. In this contribution, the tightly-coupled single-frequency multi-GNSS RTK/MEMS-IMU integration is developed to provide precise and continuous positioning solutions in urban environments. The innovation-based outlier-resistant ambiguity resolution (AR) and Kalman filtering strategy are proposed specifically for the integrated system to resist the measurement outliers or poor-quality observations. A field vehicular experiment was conducted in Wuhan City to evaluate the performance of the proposed algorithm. Results indicate that it is feasible for the proposed algorithm to obtain high-accuracy positioning solutions in the presence of measurement outliers. Moreover, the tightly-coupled single-frequency multi-GNSS RTK/MEMS-IMU integration even outperforms the dual-frequency multi-GNSS RTK in terms of AR and positioning performance for short baselines in urban environments.

Keywords: multi-GNSS (GPS/BeiDou/GLONASS); real-time kinematic (RTK); MEMS-IMU; tightly-coupled integration; urban environments; fault detection and exclusion

1. Introduction

High-accuracy positioning is an issue for many applications, such as machine control, unmanned aerial vehicles, mobile mapping, etc. For outdoor environments, Global Positioning System (GPS) real-time kinematics (RTK) has been proven to be a reliable and efficient tool because it can provide centimeter-level positioning after correctly resolving the carrier-phase integer ambiguities. Research has shown that rapid ambiguity resolution (AR) can be achieved in open sky conditions with dual-frequency GPS receivers [1], but the high-cost of dual-frequency receivers definitely makes many potential applications impossible.

Generally, the single-frequency GPS RTK has a low AR success rate and reliability [2,3]. With the rapid development of multi-GNSS [4], the performance of single-frequency RTK can be improved

significantly due to the increasing satellite visibility and better spatial geometry, as it was studied in GPS/BDS [1,5,6], GPS/GLONASS [3], GPS/BDS/GLONASS [7], and BDS/GALILEO/QZSS/GPS [8]. In this research, the combination of three main satellite navigation systems, namely the U.S. GPS, Russia's GLObal NAvigation Satellite System (GLONASS), and the Chinese BeiDou navigation satellite system (BDS), will be considered to enhance the positioning capabilities of single-frequency RTK in urban environments. Currently, both GPS and GLONASS have full constellations of thirty-two and twenty-four medium earth orbit (MEO) satellites, respectively. The Chinese BDS has begun to provide position, velocity, and timing service in the Asia-Pacific region since the end of 2012, with the constellation of five geostationary earth orbit (GEO) satellites, five inclined geo-synchronous orbit (IGSO) satellites, and four MEO satellites [4]. Different from the code division multiple access (CDMA) modulation that is adopted by GPS and BDS, GLONASS uses the frequency division multiple access (FDMA) modulation, i.e., different frequencies for different satellites [2,9]. This FDMA modulation makes GLONASS AR difficult due to the carrier phase inter-frequency bias (IFB) caused by the analog hardware delay and the digital signal processing [10]. The IFB cannot be eliminated in the double-differenced (DD) process like GPS or BDS, thus preventing the integer ambiguity resolution. Recent research has shown that the IFB can be pre-calibrated or estimated in real-time, which makes GLONASS AR possible [11,12].

In recent years, there has been increasing demand for high-accuracy positioning in urban environments. However, the RTK performance degrades in such environments due to the frequent signal blockages and multipath, even with multiple constellations. In order to provide continuous high-accuracy positioning solutions, GNSS is often integrated with INS due to their complementary characteristics [13–16]. Actually, the GPS/INS integrated system has been used in many applications that require high-accuracy position, velocity, and attitude information [14,17]. In the last few years, some researchers have investigated the positioning performance of GPS/INS integration in urban environments [18–20]. These studies were mainly based on pseudo-range and Doppler observations and only meter-level positioning accuracy could be obtained. With the rapid advances in MEMS inertial sensor technology, the low-cost GNSS/INS integration becomes increasingly attractive and suitable for many applications [21,22]. Recently, MEMS-IMUs have been integrated with low-cost GPS receivers to provide an accurate and reliable navigation solution in urban environments [23–25].

Since the GNSS measurements are easily contaminated with large multipath errors, especially for code measurements, the fault detection and exclusion (FDE) algorithm is necessary for integrated GNSS/INS system working in urban environments. Some FDE algorithms have been developed for the GPS/INS system in the literature. For example, quality control for an integrated navigation system using innovations and recursive filtering is proposed in [26]. An innovation-based detection, identification, and adaptation (DIA) procedure in an integrated navigation system is presented in [27]. In [28], a snapshot innovation method is used for improved positioning in foliage environments. Hewitson et al. extended the GNSS receiver autonomous integrity monitoring (RAIM) algorithm to the integrated GNSS/INS systems [29]. Even though these methods are effective to detect and isolate faulty measurements, a highly-reliable FDE algorithm is still needed, especially for carrier-phase-based high-accuracy positioning in GNSS-challenged environments.

Although the positioning performance in urban environments has been investigated in some previous studies, they mainly focused on the integration of GPS-only and INS, and few investigated the centimeter-level positioning capabilities in urban environments by combining the multi-GNSS data and low-cost MEMS-IMU data. In this contribution, we investigate the feasibility of high-accuracy positioning in urban environments by using the tightly-coupled integration of single-frequency GPS/BDS/GLONASS RTK and INS. The outlier-resistant AR and Kalman filtering strategy are proposed specifically for the tightly-coupled integration to resist the measurement outliers. A field vehicular experiment was conducted in Wuhan City to evaluate the AR and positioning performance of the proposed algorithm. Comparisons will be conducted with respect to the single- and dual-frequency

multi-GNSS RTK. In addition, the positioning drifts during real GNSS signal outages instead of simulated outages will be evaluated.

The paper is organized as follows: Section 2 presents the tightly-coupled multi-GNSS RTK/INS integration models including the INS dynamic model, measurement model, and single-epoch ambiguity resolution with inertial aiding. The innovation-based outlier-resistant AR and Kalman filtering strategy is also given in this section. Next, the field experiment and data processing strategies are described in Section 3. The corresponding results and discussion are presented in Section 4, followed by a summary of the work and conclusions in Section 5.

2. Methods

2.1. Tightly-Coupled GPS/BDS/GLONASS RTK/INS Integration Model

In this research, the Extended Kalman Filter (EKF) is used to implement the tightly-coupled multi-GNSS RTK/INS integration. The EKF directly fuses the multi-GNSS data and IMU data to obtain optimal estimates of the integrated system state. In order to show the tightly-coupled integration algorithm, the INS dynamic model, the measurement model and the single-epoch AR with inertial aiding will be introduced in this section.

2.1.1. INS Dynamic Model

In this research, the INS dynamic model is constructed as the $\boldsymbol{\psi}$-angle error model [30]. In this model, the error analysis is done with respect to the computer (c) frame that is locally levelled at the computed position. The $\boldsymbol{\psi}$-angle error model can be described as:

$$\begin{cases} \delta\dot{\boldsymbol{r}}^c = -\boldsymbol{\omega}_{ec}^c \times \delta\boldsymbol{r}^c + \delta\boldsymbol{v}^c \\ \delta\dot{\boldsymbol{v}}^c = \boldsymbol{f}^c \times \boldsymbol{\psi} - \left(2\boldsymbol{\omega}_{ie}^c + \boldsymbol{\omega}_{ec}^c\right) \times \delta\boldsymbol{v}^c + \delta\boldsymbol{g}^c + \mathbf{c}_b^p \delta\boldsymbol{f}^b \\ \dot{\boldsymbol{\psi}} = -\left(\boldsymbol{\omega}_{ie}^c + \boldsymbol{\omega}_{ec}^c\right) \times \boldsymbol{\psi} - \mathbf{c}_b^p \delta\boldsymbol{\omega}_{ib}^b \end{cases} \tag{1}$$

where $\delta\dot{\boldsymbol{r}}$, $\delta\dot{\boldsymbol{v}}$ and $\dot{\boldsymbol{\psi}}$ denote the time derivative of position, velocity, and attitude error vectors, respectively; $\boldsymbol{\omega}_{ie}^c$ is the angular rate of e-frame (i.e., Earth-centered, Earth-fixed (ECEF)) with respect to the inertial (i) frame, projected to the computer (c) frame; $\boldsymbol{\omega}_{ec}^c$ is the angular rate of c-frame with respect to e-frame, projected to c-frame; $\delta\boldsymbol{g}^c$ is the gravity error vector projected in the c-frame; $\delta\boldsymbol{f}^b$ and $\delta\boldsymbol{\omega}_{ib}^b$ denote the inertial sensor errors; $\mathbf{C}_b^p$ is the rotation matrix from the body (b) frame (i.e., forward-right-down (FRD)) to the platform (p) frame.

In order to improve the navigation performance of low-cost MEMS inertial sensors, the IMU errors including the bias and scale factor of both the gyroscope and accelerometer are augmented into the filter state and estimated on-line. In the implementation of GNSS/INS integration algorithms, they are generally modeled as first-order Gauss-Markov process [31]. Therefore, the complete error state vector can be described as:

$$\boldsymbol{X} = \begin{bmatrix} (\delta\boldsymbol{r}^c)^T & (\delta\boldsymbol{v}^c)^T & \boldsymbol{\psi}^T & \boldsymbol{b}_g^T & \boldsymbol{b}_a^T & \boldsymbol{s}_g^T & \boldsymbol{s}_a^T \end{bmatrix}^T \tag{2}$$

where $\delta\boldsymbol{r}^c$ and $\delta\boldsymbol{v}^c$ are position and velocity errors in the navigation frame (i.e., north-east-down (NED)), respectively; $\boldsymbol{\psi}$ is the attitude error; $\boldsymbol{b}_g$ denotes the gyro bias error; $\boldsymbol{b}_a$ denotes the accelerometer bias error; $\boldsymbol{s}_g$ and $\boldsymbol{s}_a$ are the scale factor errors of the gyro and accelerometer, respectively.

2.1.2. Measurement Model

In the single-frequency GPS/BDS/GLONASS RTK positioning, the code and carrier phase observations on f_1 frequency (herein GPS L1: 1575.42 MHz; BDS B1: 1562.098 MHz; GLONASS L1: 1602.006 + k × 0.5625 MHz, where k is the corresponding satellite frequency number) will be used together. Since there is no frequency overlap in the three GNSS systems, the double-differencing

(DD) formulation should be applied within the individual GNSS system, i.e., one reference satellite per system [5]. This is a loosely-coupled way to combine observations from different GNSS systems. The double-differenced code and carrier-phase observation equations of a single GNSS system are given as follows in units of range, and the time stamps are omitted for brevity:

$$\nabla\Delta P_R = \nabla\Delta\rho + \nabla\Delta T + \nabla\Delta I + \nabla\Delta\varepsilon_\rho \tag{3}$$

$$\lambda\nabla\Delta\varphi = \nabla\Delta\rho + \nabla\Delta T - \nabla\Delta I + \lambda\nabla\Delta N + \nabla\Delta\varepsilon_\varphi \tag{4}$$

where $\nabla\Delta(\cdot)$ denotes the DD operator; P_R and φ are code and carrier phase observations, respectively; ρ is the geometric distance in units of meters between the receiver and satellite; T and I denote the tropospheric and ionospheric delay, respectively; λ and N are carrier phase wavelength and integer ambiguity, respectively; ε_ρ and ε_φ are the measurement noise and un-modeled residual error (multipath, etc.) of code and carrier phase observations, respectively. Specifically, for GLONASS carrier phase observations, $\lambda\nabla\Delta\varphi$ and $\lambda\nabla\Delta N$ could be written as follows:

$$\lambda\nabla\Delta\varphi = \lambda^k\Delta\varphi^k - \lambda^r\Delta\varphi^r \tag{5}$$

$$\lambda\nabla\Delta N = \lambda^k\Delta N^k - \lambda^r\Delta N^r = \lambda^k\nabla\Delta N^{kr} + (\lambda^k - \lambda^r)\Delta N^r \tag{6}$$

where the superscripts k and r denote the non-reference and reference satellite, respectively; $\Delta(\cdot)$ represents the single-differenced (SD) operator. In Equation (6), the SD ambiguity can be estimated with the SD pseudo-range observations [32]. As the observation of low-elevation satellite is generally noisier, the elevation-dependent weight model is adopted to determine the *a priori* variance for GNSS observations [33]:

$$\sigma^2 = \begin{cases} \sigma_0^2, \; ele \geq \pi/6 \\ (\sigma_0/\sin(ele))^2, \; else \end{cases} \tag{7}$$

where σ_0 is the un-differenced observation standard deviation (STD) at zenith, and ele is the elevation angle.

For RTK positioning of short baseline, the tropospheric term T and ionospheric term I in Equations (3) and (4) can be neglected. The remaining unknown parameters that need to be estimated are the baseline increment vector and integer ambiguities. For single-frequency GPS/BDS/GLONASS RTK, the linearized DD observation with unknown parameters can be described in matrix form as follows:

$$\begin{bmatrix} \boldsymbol{\varepsilon}_\rho \\ \boldsymbol{\varepsilon}_\varphi \end{bmatrix} = \begin{bmatrix} \boldsymbol{H} & \mathbf{0}_{n\times n} \\ \boldsymbol{H} & \boldsymbol{\Lambda} \end{bmatrix} \begin{bmatrix} \delta\boldsymbol{p}_r \\ \nabla\Delta\boldsymbol{N} \end{bmatrix} - \begin{bmatrix} \nabla\Delta\boldsymbol{P}_R - \nabla\Delta\boldsymbol{r}_0 \\ \lambda\nabla\Delta\boldsymbol{\varphi} - \nabla\Delta\boldsymbol{r}_0 \end{bmatrix} \tag{8}$$

with

$$\boldsymbol{H} = \begin{bmatrix} \boldsymbol{H}^G & \boldsymbol{H}^C & \boldsymbol{H}^R \end{bmatrix}^T \tag{9}$$

$$\boldsymbol{\Lambda} = diag\begin{pmatrix} \boldsymbol{\Lambda}^G & \boldsymbol{\Lambda}^C & \boldsymbol{\Lambda}^R \end{pmatrix} \tag{10}$$

$$\boldsymbol{N} = \begin{bmatrix} \boldsymbol{N}^G & \boldsymbol{N}^C & \boldsymbol{N}^R \end{bmatrix}^T \tag{11}$$

where n is the total number of DD ambiguities; $\delta\boldsymbol{p}_r$ is the baseline increment vector; $\nabla\Delta\boldsymbol{r}_0$ denotes the computed DD ranges with approximate rover coordinates and satellite positions; the superscripts 'G', 'C', 'R' represent GPS, BDS and GLONASS, respectively; $\boldsymbol{H}$ is the design matrix containing the relative receiver-satellite geometry; $\boldsymbol{\Lambda}$ is the diagonal matrix that contains the wavelengths of f_1 frequencies from the GPS, BDS and GLONASS satellites.

For the tightly-coupled integration, the measurement model in the discrete-time form can be expressed as

$$\boldsymbol{Z}_k = \boldsymbol{H}_k\boldsymbol{X}_k + \boldsymbol{V}_k \tag{12}$$

where $\boldsymbol{H}_k$ is the design matrix, and $\boldsymbol{Z}_k$ is the measurement vector with the following formula:

$$\boldsymbol{Z}_k = \begin{bmatrix} \nabla\Delta\hat{\boldsymbol{\rho}}_{INS} - \nabla\Delta\boldsymbol{P}_{R,GNSS} \\ \nabla\Delta\hat{\boldsymbol{\rho}}_{INS} - \lambda\nabla\Delta\boldsymbol{\varphi}_{GNSS} \end{bmatrix} \tag{13}$$

where the subscripts "INS" and "GNSS" represent the INS-predicted ranges and GNSS observations, respectively. The INS-predicted ranges are calculated using the INS-updated position and satellite positions.

Since the IMU measurement center and the GNSS antenna phase center cannot be installed at the same place, the lever-arm offset should be considered when fusing the two different kinds of data. The lever-arm correction can be described in the *e*-frame as:

$$\boldsymbol{r}^e_{GNSS} = \boldsymbol{r}^e_{IMU} + \boldsymbol{C}^e_n \boldsymbol{C}^n_b \boldsymbol{\ell}^b_{GNSS} \tag{14}$$

where $\boldsymbol{r}^e_{GNSS}$ and $\boldsymbol{r}^e_{IMU}$ are position coordinates in the *e*-frame for the GNSS rover receiver and IMU center, respectively; $\boldsymbol{C}^e_n$ is the rotation matrix form the *n*-frame to the *e*-frame; $\boldsymbol{C}^n_b$ is the rotation matrix form the *b*-frame to the *n*-frame; $\boldsymbol{\ell}^b_{GNSS}$ denotes the lever-arm offset vector in the *b*-frame. After the error perturbation analysis, the position error term between the IMU and GNSS antenna can be written as [34]:

$$\delta\boldsymbol{r}^e_{GNSS} \approx \delta\boldsymbol{r}^e_{IMU} + \boldsymbol{C}^e_n \left[\left(\boldsymbol{C}^n_b \boldsymbol{\ell}^b_{GNSS} \right) \times \right] \boldsymbol{\psi} \tag{15}$$

where $\times$ denotes the cross-product operator. Considering that the position error term in the system state vector is expressed in the *n*-frame, the final design matrix $\boldsymbol{H}_k$ in (12) can be derived from (3), (4), (9), (13), and (15) as:

$$\boldsymbol{H}_k = \begin{bmatrix} \boldsymbol{H} \cdot \boldsymbol{C}^e_n & \boldsymbol{0}_{n\times 3} & \boldsymbol{H} \cdot \boldsymbol{C}^e_n \cdot \left[\left(\boldsymbol{C}^n_b \boldsymbol{\ell}^b_{GNSS} \right) \times \right] & \boldsymbol{0}_{n\times 12} \end{bmatrix} \tag{16}$$

2.1.3. Single-Epoch Ambiguity Resolution with Inertial Aiding

Differential carrier-phase based centimeter-level positioning relies on the correct integer ambiguity resolution, but there are still challenges for reliable ambiguity resolution in urban environments, especially for single-frequency RTK. For the tightly-coupled RTK/INS integration, a priori information from INS can be used to reduce the search space of integer ambiguities, and then improve the AR reliability [35]. In this research, the INS predicted position information is used as a virtual measurement. Assuming that the observation equation is linearized at the INS predicted position, and then the virtual observation equation from INS predicted position can be written as:

$$\boldsymbol{\varepsilon}_{INS} = \begin{bmatrix} \boldsymbol{I}_{3\times 3} & \boldsymbol{0}_{3\times n} \end{bmatrix} \begin{bmatrix} \delta\boldsymbol{p}_r \\ \nabla\Delta\boldsymbol{N} \end{bmatrix} - \boldsymbol{0}_{3\times 1} \tag{17}$$

where $\boldsymbol{I}_{3\times 3}$ is the identity matrix. Combining the above equation and (8), the unknown parameters and their corresponding covariance can be obtained through the weighted least-squares estimation:

$$\left(\boldsymbol{B}^T \boldsymbol{W} \boldsymbol{B} \right) \begin{bmatrix} \delta\boldsymbol{p}_r \\ \nabla\Delta\boldsymbol{N} \end{bmatrix} = \boldsymbol{B}^T \boldsymbol{W} \boldsymbol{L} \tag{18}$$

with:

$$\boldsymbol{B} = \begin{bmatrix} \boldsymbol{H} & \boldsymbol{0}_{n\times n} \\ \boldsymbol{H} & \lambda\boldsymbol{I}_{n\times n} \\ \boldsymbol{I}_{3\times 3} & \boldsymbol{0}_{3\times n} \end{bmatrix}, \ \boldsymbol{W} = \boldsymbol{diag}\begin{pmatrix} \boldsymbol{W}_\rho & \boldsymbol{W}_\varphi & \boldsymbol{W}_{INS} \end{pmatrix}, \ \boldsymbol{L} = \begin{bmatrix} \nabla\Delta\boldsymbol{P}_R - \nabla\Delta\boldsymbol{r}_0 \\ \lambda\nabla\Delta\boldsymbol{\varphi} - \nabla\Delta\boldsymbol{r}_0 \\ \boldsymbol{0}_{3\times 1} \end{bmatrix}$$

where $\boldsymbol{W_\rho}$, $\boldsymbol{W_\varphi}$, and $\boldsymbol{W_{INS}}$ are the inverse of the covariance matrices of the code, carrier phase, and INS virtual measurements, respectively. Further, the coefficient matrix of the normal Equation (18) can be derived as follows:

$$\boldsymbol{B}^T\boldsymbol{W}\boldsymbol{B} = \begin{bmatrix} \boldsymbol{H}^T\boldsymbol{W_\rho}\boldsymbol{H} + \boldsymbol{H}^T\boldsymbol{W_\varphi}\boldsymbol{H} + \boldsymbol{W_{INS}} & \lambda\boldsymbol{H}^T\boldsymbol{W_\varphi} \\ \lambda\boldsymbol{W_\rho} & \lambda^2\boldsymbol{W_\rho} \end{bmatrix} \tag{19}$$

Generally, the strength of the normal equation is weak if the code and carrier phase observations are used only because the code measurements are imprecise. With the term $\boldsymbol{W_{INS}}$ in the top-left corner of the above equation, the strength will be enhanced and then the accuracy of the float solution can be improved. Since the precision of INS predicted position is high in the short-term period, this virtual measurement will definitely improve the AR performance.

Once the real-valued ambiguities and their corresponding variance-covariance (VC) matrix are obtained, the Least-squares AMBiguity Decorrelation Adjustment (LAMBDA) method is performed to obtain the integer-valued ambiguities [36]. Then, the ambiguity validation test is performed to determine whether the searched ambiguities should be accepted or not. The validation test is very crucial, as incorrect ambiguity resolution will lead to unacceptable positioning result. In practice, the data-driven ratio-test and model-driven bootstrapped success rate are used together for ambiguity validation [37,38], which will be adopted in this research as well.

2.2. Innovation-Based Outlier-Resistant Ambiguity Resolution and Kalman Filtering Strategy

In order to keep the optimality of the system state, faulty measurements should be excluded before the Kalman updates. In urban environments, the code and carrier phase observations are susceptible to multipath errors, especially for the code measurements. In the tightly-coupled RTK/INS integration, large code multipath errors will bias the estimates of the float ambiguities dramatically and then reduce the probability of correctly fixing the ambiguities. To reduce the effects of measurement outlier on the parameter estimation, the observation variance should be inflated properly for those with outliers.

Under normal operating condition, the measurement innovation sequence of Kalman filtering should be normally distributed with zero mean. When discrepancies in innovation sequence are found, the faulty measurements are detected. In this research, the following innovation-based inflating factor γ_{ii} is constructed to model the measurements [39]:

$$\gamma_{ii} = \begin{cases} 1, \ \left|\widetilde{v}_{k,i}\right| \le k_0 \\ \frac{\left|\widetilde{v}_{k,i}\right|}{k_0} \times \left(\frac{k_1 - k_0}{k_1 - \left|\widetilde{v}_{k,i}\right|}\right), k_0 < \left|\widetilde{v}_{k,i}\right| \le k_1 \\ \infty, \left|\widetilde{v}_{k,i}\right| > k_1 \end{cases} \tag{20}$$

where k_0 and k_1 are two constants, usually chosen as 2.0–3.0 and 4.5–8.5, respectively; $\widetilde{v}_{k,i}$ is the i-th normalized measurement innovation at epoch k, which can be written as:

$$\widetilde{v}_{k,i} = \frac{V_{k,i}}{\sqrt{\left(\boldsymbol{H}_k\boldsymbol{P}_{k,k-1}\boldsymbol{H}_k^T + \boldsymbol{R}_k\right)_{i,i}}} \tag{21}$$

where $V_{k,i}$ is the i-th measurement innovation at epoch k; $\boldsymbol{P}_{k,k-1}$ is the time update of covariance matrix in the Kalman filtering; $\boldsymbol{R}_k$ is the measurement covariance matrix. In Equation (20), γ_{ii} is equal to one if the measurement is normal; when the measurement is outlying, γ_{ii} is infinite, i.e., this gross measurement will be eliminated; when the normalized value is between k_0 and k_1, the effect of this measurement on the parameter estimation will be reduced.

Since the DD measurements are correlated mathematically, the inflated measurement covariance matrix should preserve the original correlation. Therefore, the following equivalent covariance matrix should be used in the measurement update:

$$\overline{\boldsymbol{R}}_k = \begin{bmatrix} \gamma_{11}\sigma_1^2 & \cdots & \gamma_{1n}\sigma_{1n} \\ \vdots & \ddots & \vdots \\ \gamma_{n1}\sigma_{n1} & \cdots & \gamma_{nn}\sigma_n^2 \end{bmatrix} \tag{22}$$

with:

$$\gamma_{ij} = \sqrt{\gamma_{ii}\gamma_{jj}} \tag{23}$$

where γ_{ij} is the inflating factor of the covariance at i-th row and j-th column.

In the ambiguity resolution process, the outlier-resistant scheme will be applied to model the code measurements so that the effects of the abrupt measurement errors on the float ambiguities can be eliminated. In the measurement update stage of Kalman filter, the outlier-resistant filtering will be activated again to model the code or ambiguity-fixed carrier phase observations in case of wrongly accepted ambiguities. With the outlier-resistant ambiguity estimation and filtering, the unbiased float ambiguities and system states can be achieved; otherwise, the system states may become biased or even make the integration filter diverged. Obviously, the two-step outlier-resistant scheme is easy to implement in the framework of RTK/INS integration and little extra computation is required.

2.3. Overview of Multi-GNSS RTK/INS Tightly-Coupled Integration with Innovation-Based FDE

According to the description above, an overview of the proposed multi-GNSS RTK/INS integration with innovation-based FDE is shown in Figure 1. After the system initialization, the compensated raw IMU outputs are used in the INS mechanization to provide high data-rate position, velocity and attitude (PVA) information. In the process of INS mechanization, the second-order coning correction term, the rotational and sculling motion effect are considered to weaken their influences on the attitude and velocity update [40,41].

Once the multi-GNSS data from base and rover receivers are available, the double-differenced code and carrier phase observations will be formed within the individual GNSS system. Then, the outlier-resistant ambiguity resolution with INS aiding will be used to resist the code measurement outliers. The LAMBDA method is employed for ambiguity resolution, and a validation process will be used to confirm the correctness of the fixed ambiguities. If the searched ambiguities pass the validation test, the precise ambiguity-fixed carrier phase measurements will be used to update the tightly-coupled integration filter; otherwise, the code observations should be used at this epoch. The measurement inputs of the integration filter is the difference between INS-derived DD ranges and DD code or carrier-phase observations. In the EKF update phase, the outlier-resistant filtering is applied again to model the potential code measurement outlier or the ambiguity-fixed carrier phase measurement in case the incorrectly-fixed ambiguities are accepted. Since the output rate of IMU data is much higher than that of GNSS data, the standalone INS mode will process the IMU data epoch-by-epoch when the GNSS data is not available.

Finally, the estimated IMU sensor errors including the biases and scale factors of the gyroscope and accelerometer are fed back to compensate the errors of raw IMU data. Meanwhile, the navigation solution provided by INS mechanization is updated with the estimated PVA errors from the integration filter.

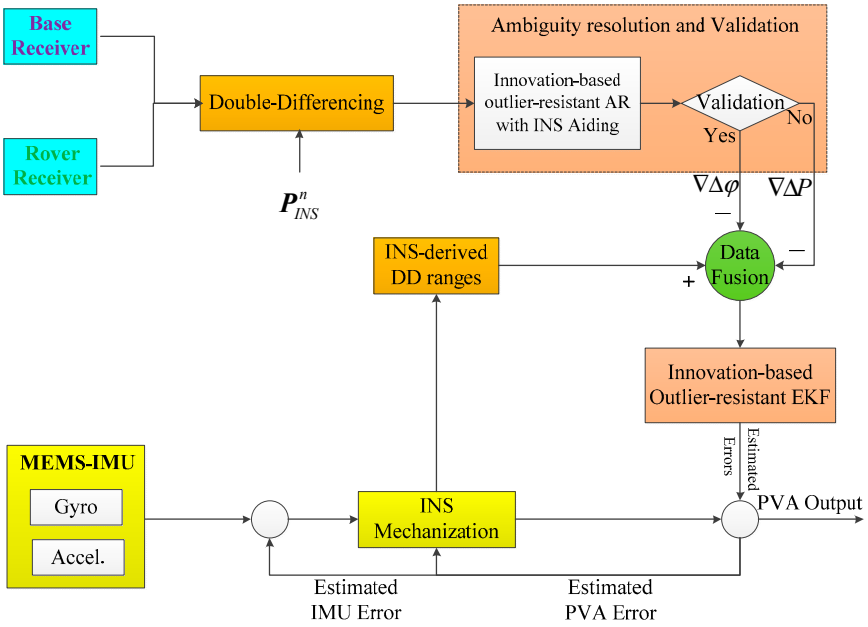

Figure 1. Implementation of the innovation-based outlier-resistant ambiguity resolution and Kalman filtering for the tightly-coupled integration of multi-GNSS RTK and MEMS-IMU.

3. Field Test Description and Data Processing Strategy

In order to evaluate the performance of the proposed robust single-frequency multi-GNSS RTK/MEMS-IMU integration in urban environments, a field vehicular test was carried out in Wuhan City, China on 12 June 2015. The trajectory, as shown in Figure 2a, is about 7.0 km in the north-south direction and 7.2 km in the east-west direction. A range of scenarios was incorporated in the test route, including relatively open-sky condition, under trees and overpasses, and sub-dense urban canyon with high buildings (Figure 2b). Figure 2c shows the test platform and equipment used in this paper. The inertial data from MEMS grade IMU (POS1100), which consists of three MEMS gyroscopes and three quartz accelerometers, was used in this research. The tactical-grade IMU (POS310) with three fiber optic gyroscopes (FOGs) was used to provide the reference solutions. Both of the two IMUs are provided by Wuhan MaiPu Space Time Technology Company (Wuhan, China), and their output rate are 200 Hz. Their main performance specifications are shown in Table 1.

A Trimble NetR9 multi-GNSS receiver (Sunnyvale, CA, USA), as the reference station, was located on the rooftop of the GNSS Research Center at Wuhan University to collect raw GNSS data. The rover receiver (Trimble BD982 OEM board) was fixed on the vehicle during the driving test. The lever arm offset between the phase center of the rover GNSS antenna and the IMU measuring center was accurately measured in advance. In the experiment, the sampling rate of multi-GNSS data in the base and rover station was set to 1 Hz. As shown in Figure 2d, the field test took about 45 min and the vehicle stayed static in the first several minutes.

In the data processing, broadcast ephemeris are used to provide satellite clocks and orbits for GPS, BDS, and GLONASS. As the baseline separation is less than 7 km, the tropospheric and ionospheric delay are not considered. Empirically, a priori standard deviations for the un-differenced GPS, BDS, and GLONASS carrier phase observation at the zenith are set to 3 mm. The values for code observations of GPS, BeiDou MEO/IGSO, BeiDou GEO, and GLONASS satellites are 0.35 m, 0.35 m, 0.5 m, and 0.5 m, respectively. In terms of the ambiguity validation, the predefined success rate is set to 0.99, and the critical ratio value is 3.0 for the GPS-only and 2.0 for the combined GNSS system. The main reason why smaller ratio value is applied to the combined GNSS system is that it provides much better satellite geometry and model strength for reliable AR than the single GNSS system [42].

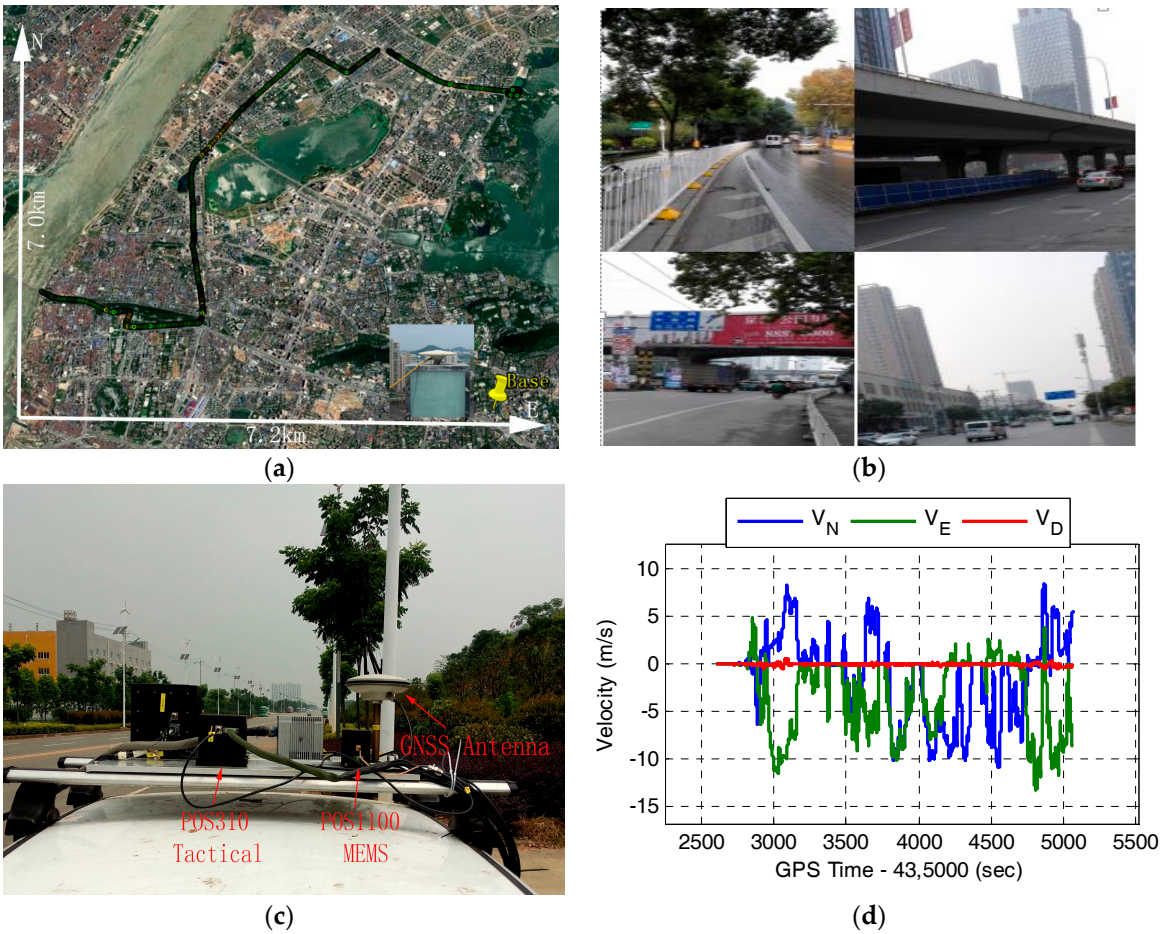

Figure 2. Test description of the land vehicle experiment on 12 June 2015 in Wuhan, China. (**a**) Test trajectory; (**b**) typical scenarios; (**c**) platform and equipment; and (**d**) vehicle speed in the field test.

Table 1. Performance specifications of the IMU sensors in the experiment.

IMU	Grade	Dimensions (mm)	Bias		Random Walk	
			Gyro. ($^\circ/h$)	Acce. (mGal)	Angular ($^\circ/\sqrt{h}$)	Velocity ($m/s/\sqrt{h}$)
POS310	Tactical	151 × 120 × 101	0.5	300	0.05	0.10
POS1100	MEMS	81.8 × 68 × 70	10.0	1500	0.33	0.18

4. Results and Discussion

4.1. Satellite Availability

The satellite availability in sub-dense urban environments is investigated at first for the GPS (G), BDS (C) and GLONASS (R). As shown in Figure 3, the PRN numbers between 1 and 32 are for the GPS satellites, between 33 and 67 for the BDS, and between 68 and 91 for the GLONASS. Currently, the constellations of GPS and GLONASS consist of MEO satellites only, whereas the BDS constellation is comprised of GEO, IGSO, and MEO satellites. In this field test, there are four GEO satellites (C33, C35, C36, and C37) and five IGSO satellites (C38–C42) tracked, but no MEO satellites were tracked. It can be seen that some satellites' tracking conditions are very poor due to the high buildings and overpasses in the urban environments wherein the longest partial GNSS outage lasted about 2 min with only 1–2 satellites tracked. Obviously, the multi-GNSS provides many more available satellites than the GPS only, which will definitely bring benefits for RTK positioning in urban environments.

The number of satellites and the corresponding position dilution of precision (PDOP) of GPS, GPS + BDS (G + C), and GPS + BDS + GLONASS (G + C + R) with a 15° cut-off elevation angle in the rover station are depicted in Figure 4a,b, respectively.

It can be seen from Figure 4 that the satellite availability and PDOP can be improved visibly by using the combined GPS/BDS and GPS/BDS/GLONASS systems. According to the statistics from Figure 4, the average number of satellites of GPS, GPS + BDS, and GPS + BDS + GLONASS are 6.0, 12.3, and 16.5, and the corresponding average PDOPs are 3.12, 2.05, and 1.71, respectively. Compared with the GPS, the PDOP improvements of the multi-GNSS are about 34.3–45.2%. Obviously, the average number of available satellites in urban environments are less than that in open-sky conditions.

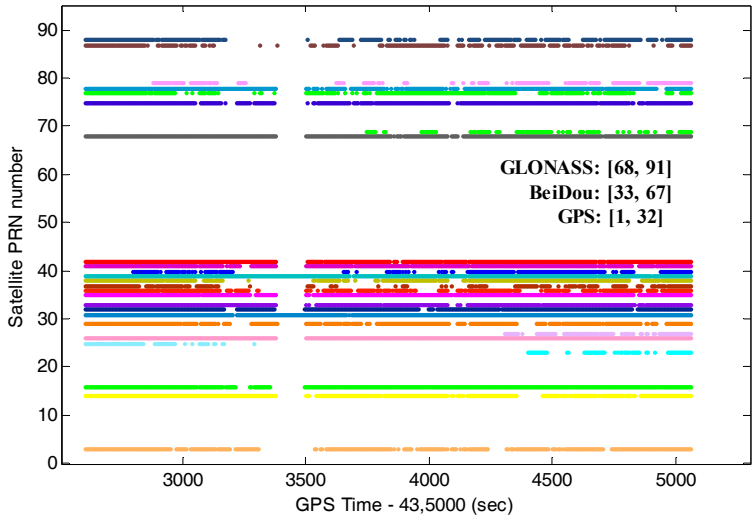

Figure 3. Satellite availability of GPS ($1 \leq$ PRN ≤ 32), BeiDou ($33 \leq$ PRN ≤ 67), and GLONASS ($68 \leq$ PRN ≤ 91) with a 15° cut-off elevation angle.

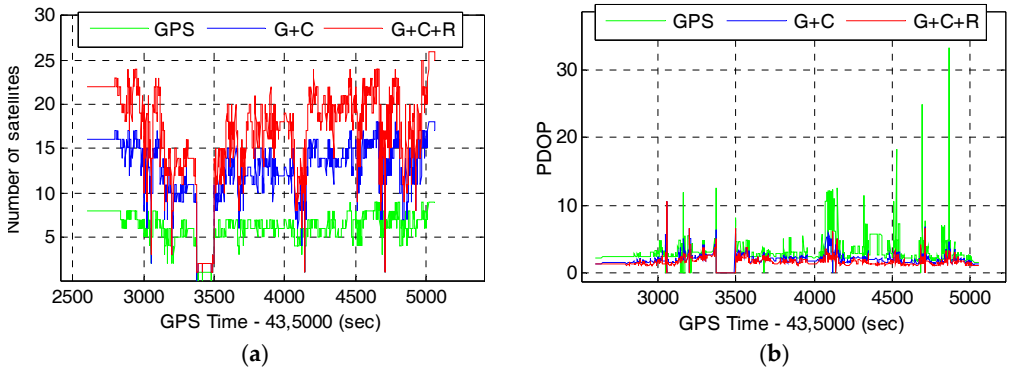

Figure 4. The number of available satellites and PDOP of GPS (G), GPS/BDS (G + C), and GPS/BDS/GLONASS (G + C + R) with a 15° cut-off elevation angle in the rover station. (**a**) Number of satellites; and (**b**) PDOP.

4.2. Multi-GNSS RTK/INS Integration with Innovation-Based FDE

One of the key issues for GNSS-based high-accuracy positioning in urban environments is the fault detection and exclusion because the GNSS observations are more likely to contain measurement outliers. As the code measurements can have very large multipath error, they should be detected and excluded in the data processing. As stated previously, the measurement innovations of Kalman filtering should be distributed with zero mean and there will be discrepancies for those measurements with outliers. Figure 5 depicts the code innovations for all available GPS + BDS + GLONASS satellites

with a 15° cut-off elevation angle. It can be seen that very large code measurement outliers (shown in three red circles) are detected in the Kalman filter's innovation sequence of DD code observation. A zoom-in window is given to show the spread of those code innovations with small magnitudes. It shows that most of the code innovations are within ±2 m, but there are still small discrepancies. There is no doubt that these code measurements with abrupt outliers will affect ambiguity resolution and positioning accuracy if no effective measures are taken.

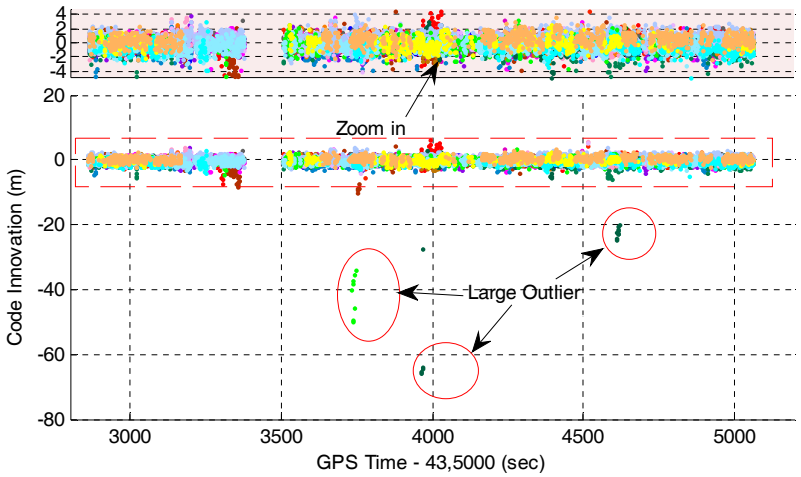

Figure 5. Kalman filter's innovation sequence of double-differenced code observation for all available GPS + BDS + GLONASS satellites with a 15° cut-off elevation angle. Each color denotes a different satellite pair. The points in three red circles are very large code measurement outliers.

Figure 6 gives an example about the effects of code measurement outlier on the estimation of float ambiguities. It shows the ambiguity biases with and without innovation-based FDE in the presence of one code measurement outlier on a GLONASS satellite whose code innovation is –19.8 m (given by the integration filter). The ambiguity bias is defined as the difference between the estimated float ambiguity and its true integer value. If the ambiguity bias is closer to zero, it is more likely to fix the ambiguity correctly. It can be seen that the ambiguity biases are within 0.15 cycles, except the satellite with the outlier (about 0.26 cycles), when the innovation-based FDE strategy is applied. By comparison, the ambiguity biases are much larger without FDE and the maximum ambiguity bias is even more than 0.6 cycles, which will prevent correct ambiguity fixing.

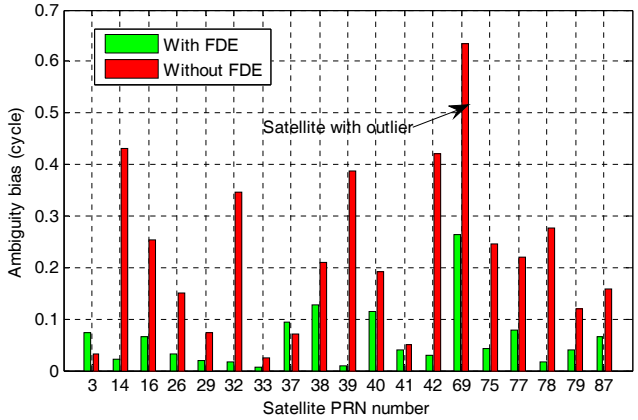

Figure 6. Ambiguity biases with and without innovation-based FDE in the presence of one code measurement outlier on a GLONASS satellite at epoch 439,618 s (The PRN number is 69 with an elevation of 21.4°, and the DD code innovation given by the integration filter is −19.8 m).

In order to verify the feasibility of high-accuracy positioning in the presence of measurement outliers, Figure 7 shows the root-mean-square (RMS) of code innovations of the tightly-coupled GPS/BDS/GLONASS/INS integration and the AR fixing differences with and without innovation-based FDE. The epochs whose AR fixing difference is equal to zero (shown in red) means that the fixing states of these epochs are the same, i.e., both fixed or float. The epochs that can be fixed only with FDE are depicted with green circles. It can be seen that the ambiguity-fixed solution can be obtained in some cases even though a large code measurement outlier is present. Clearly, the innovation-based FDE strategy is effective to resist the code measurement outliers and, thus, improve the ambiguity resolution performance.

Since the ambiguity is resolved in the single-epoch mode, the integrated filter will be insensitive to the frequent cycle slips in urban environments. In the filter's measurement update stage, the outlier-resistant Kalman filtering strategy will be applied for the code or ambiguity-fixed carrier-phase measurements. For carrier-phase based high-accuracy positioning, the ambiguity-fixed carrier phase residual can indicate the correctness of ambiguity resolution and positioning accuracy. Figures 8 and 9 show the DD carrier phase residual and the corresponding RMS of all the available satellites of the tightly-coupled GPS/BDS/GLONASS/INS integration, respectively.

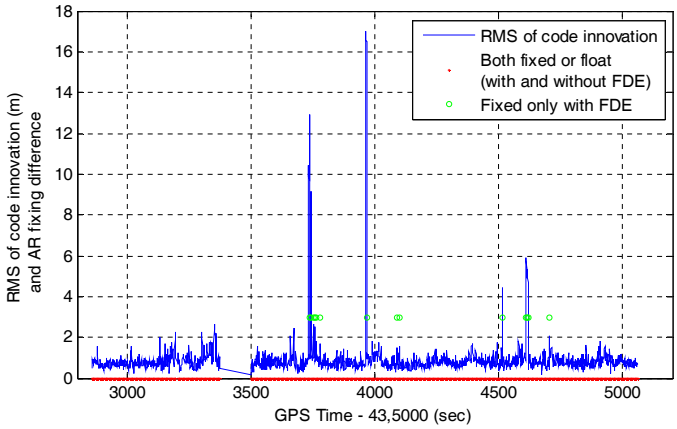

Figure 7. RMS of code innovations for the tightly-coupled GPS/BDS/GLONASS/INS integration and the AR fixing difference with and without FDE.

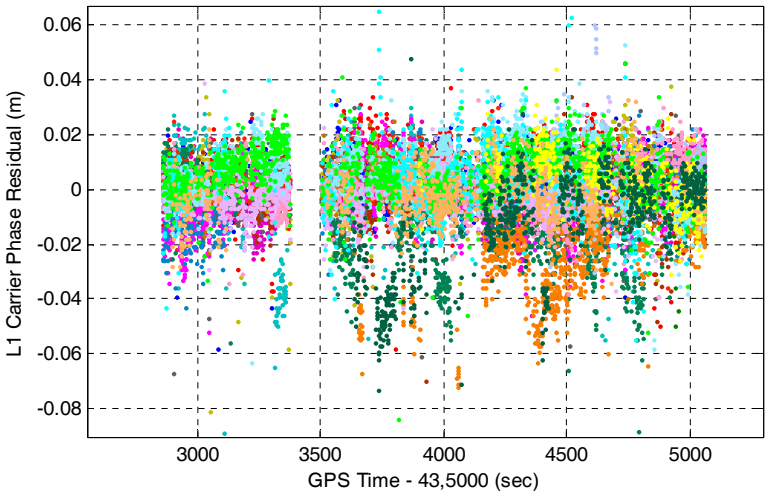

Figure 8. DD carrier phase residual for the tightly-coupled GPS/BDS/GLONASS/INS integration. Each color denotes a different satellite pair. (Measurement noise, multipath, and atmospheric delay are included).

It can be seen from Figure 8 that the DD carrier phase residuals are below 10 cm for all the available satellites and most of them are within ±2 cm. The obvious discrepancies of some residuals may be mainly due to the un-modeled multipath effects. The corresponding RMSs of carrier phase residuals are below 20 mm, except for one BDS IGSO satellite and one GLONASS satellite (shown in Figure 9). The relatively large residuals of these two satellites may be caused by low-elevation multipath.

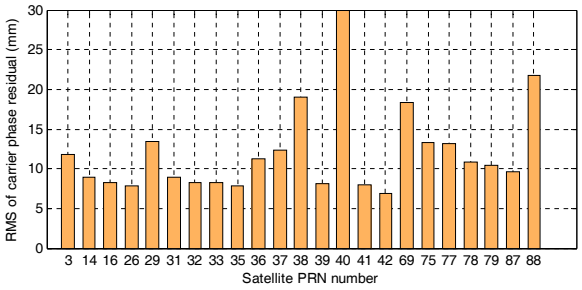

Figure 9. RMS of the DD carrier phase residual for the tightly-coupled GPS/BDS/GLONASS/INS integration.

4.3. Single-Epoch Ambiguity Resolution and Positioning

In order to assess the AR and positioning performance of the single-frequency multi-GNSS RTK/INS tightly-coupled integration algorithm in urban environments, the reference trajectory was generated firstly by using the measurements of a tactical-grade POS310 IMU and dual-frequency GPS/BDS/GLONASS data in the tightly-coupled RTK/INS integration mode with Rauch-Tung-Striebel (RTS) smoothing [43]. Since frequent loss-of-lock occurs in urban environments, we focus on the single-epoch ambiguity resolution and positioning performance in this research. This method has the advantage that the positioning results are insensitive to the cycle slips. The ambiguity resolution and positioning performance of single- and dual-frequency RTK (single GPS and multi-GNSS) will also be investigated and their results will be compared with the solution of the tightly-coupled single-frequency RTK/INS integration. In order to show the difference of RTK with and without INS aiding, the positioning results of the tightly-coupled RTK/INS integration are excluded at those epochs when the GNSS-only solution is not available (e.g., the number of satellites is less than four for GPS).

We first evaluate the AR and positioning performance of the GPS, GPS + BDS (G + C), and GPS + BDS + GLONASS (G + C + R) with a customary cut-off elevation angle of 15°. Figure 10 shows the time series of position difference in the north, east, and vertical directions for single-frequency RTK (GPS, G + C, G + C + R, top two rows), dual-frequency RTK (GPS, G + C, G + C + R, middle two rows), and single-frequency RTK/INS integration (GPS, G + C, G + C + R, bottom two rows). The correctly-fixed solutions, incorrectly-fixed solutions, and float solutions are shown in green, red, and grey, respectively. The zoom-in windows are provided for both the horizontal (north, east) scatterplots and vertical (down) time series to show the details of the correctly-fixed solutions. The correctness of ambiguity fixing is checked according to the positioning difference between the fixed solution and the reference solution. If the position difference is larger than 0.1 m in the north or east components, or 0.15 m in the vertical direction, the integer ambiguities will be considered as incorrectly fixed.

It can be seen from Figure 10 that the AR and positioning performance of single-frequency GPS-only RTK is very poor, indicating that it is difficult to use single-frequency GPS RTK for high-accuracy kinematic positioning in urban environments. The addition of BDS increases the AR performance dramatically, and the inclusion of GLONASS together further improves the performance. Compared with the single-frequency GPS RTK, the dual-frequency GPS RTK can obviously improve the positioning performance due to the doubled observations on another frequency, but its performance is worse than the single-frequency multi-GNSS RTK. Therefore, better satellite availability from

multi-GNSS brings benefits for single-frequency RTK in urban environments. Significantly, the AR and positioning performance of dual-frequency multi-GNSS RTK are further improved with a substantial decrease of ambiguity-float solutions in comparison with the single-frequency multi-GNSS RTK.

The results from Figure 10 also show that the ambiguity resolution and positioning performance of the single-frequency multi-GNSS RTK/INS integration can be significantly improved with fewer ambiguity-float solutions than the corresponding single- and dual-frequency RTK solutions. Compared with single-frequency GPS RTK, the corresponding tightly-coupled GPS RTK/INS integration has only small improvements in AR performance, but the accuracy and stability of the ambiguity-float position series improves significantly due to the short-term accuracy and strong constraints of the INS. For kinematic positioning in urban environments, this is one of the most important advantages of the integrated GNSS/INS system. In case of RTK positioning, the ambiguity-float position error can be large because it mainly depends on the quality and precision of the code measurements.

In Table 2, we provide the corresponding statistical information in terms of RMS of position difference of the float and correctly-fixed single-epoch solution, positioning availability and fixing rate of GPS, GPS + BDS, and GPS + BDS + GLONASS. The position availability, i.e., the percentage of all epochs that the RTK positioning, is available to the total number of epochs. The AR fixing rate for full ambiguity resolution was computed by:

$$P_{FR} = \frac{number\ of\ correctly\ fixed\ epochs}{total\ number\ of\ epochs} \tag{24}$$

For the single-epoch-based kinematic positioning, this fixing rate directly reflects the high-accuracy positioning availability.

It can be seen from Table 2 that the positioning availability is increased from 85.5% of the GPS to 91.8% of the GPS + BDS and 92.4% of the GPS + BDS + GLONASS, respectively. The fixing rate of the single-frequency GPS RTK is only 0.1%. By comparison, the fixing rate of single-frequency GPS + BDS and GPS + BDS + GLONASS RTK increases to 25.1% and 44.7%, respectively. Obviously, the dual-frequency multi-GNSS RTK greatly improves the AR performance with fixing rates of 75.8% and 76.7% for the GPS + BDS and GPS + BDS + GLONASS systems, respectively. The dual-frequency GPS-only RTK has a low fixing rate of 10.4% due to the poor satellite geometry (mean number of satellites is 6.0). The single-frequency multi-GNSS RTK/INS integration shows better AR performance with fixing rate of 86.1% for both the GPS + BDS and GPS + BDS + GLONASS system. This means that centimeter-level positioning accuracy is available over 86% of the time in the field test with the tightly-coupled single-frequency multi-GNSS RTK/INS integration. Similar to the dual-frequency GPS-only RTK, the fixing rate of single-frequency GPS RTK/INS integration is also very low (only 5.8%).

Table 2. The positioning availability (*PA*, %), RMS of positioning differences (north, east, down) of the float and correctly-fixed single-epoch solution, and fixing rate P_{FR}(%) for different system configurations with a 15° cut-off elevation angle.

System	**G**				**G + C**				**G + C + R**			
PA	**85.5**				**91.8**				**92.4**			
RMS (cm)	**N**	**E**	**D**	**FR**	**N**	**E**	**D**	**FR**	**N**	**E**	**D**	**FR**
L1 RTK	0.35	0.45	1.58	0.1	1.27	2.21	2.09	25.1	0.35	0.38	1.13	44.7
Fixed/Float	105.9	97.2	179.0		74.42	76.27	180.9		83.54	86.67	188.9	
L1 + L2 RTK	0.72	0.74	1.47	10.4	0.57	0.62	1.59	75.8	0.57	0.56	1.41	76.7
Fixed/Float	91.19	90.88	147.1		81.66	95.23	170.9		86.83	91.90	143.9	
L1 + INS	1.60	1.60	1.45	5.8	0.55	0.65	1.79	86.1	0.53	0.57	1.50	86.1
Fixed/Float	58.40	34.94	85.61		23.54	37.35	53.61		16.44	27.78	44.81	

The results from Table 2 also show that the RMSs of the position differences of the correctly-fixed solutions for the GPS, GPS + BDS, and GPS + BDS + GLONASS are all within 3 cm in the north,

east, and vertical directions. Noticeably, the RMSs of the float solutions of the tightly-coupled single-frequency RTK/INS integration are much smaller than that of the single- and dual-frequency RTK. We also notice that some RMS values of the L1-RTK fixed solutions are smaller than that of L1/L2-RTK. The main reason for this is that the fixing rate of L1-RTK is much lower and the majority of these fixed solutions are obtained under relatively good observation conditions with small PDOP and multipath error. Therefore, the precision of these fixed solutions can be very high and the RMS value of them is smaller. Similarly, the reason why some RMS values of L1/L2-RTK float solutions is greater than that of L1 RTK is that the percentage of L1/L2 float solutions is much lower and the observation condition of these epochs is generally very poor with fewer visible satellites. Overall, the L1 RTK can obtain fixed solutions in good condition while L1/L2 RTK can obtain fixed solutions in more challenged cases.

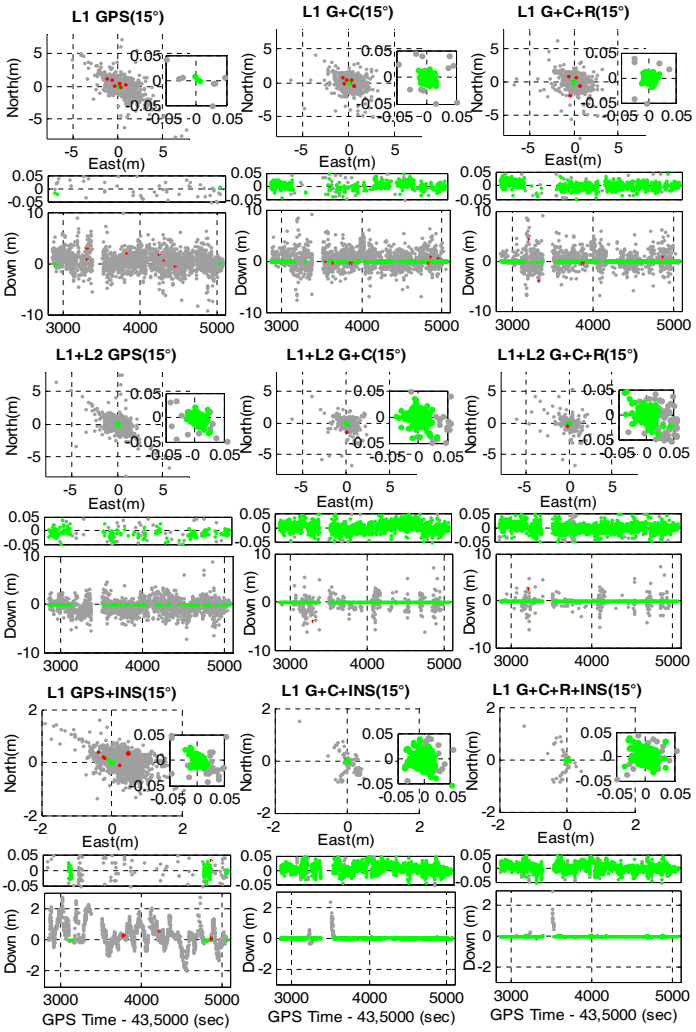

Figure 10. Time series of position difference in the north, east, and vertical directions for GPS (1st column), GPS + BDS (G + C, 2nd column) and GPS + BDS + GLONASS (G + C + R, 3rd column) with a 15° cut-off elevation angle. The top two rows are single-frequency RTK (GPS, G + C, and G + C + R). The middle two rows are dual-frequency RTK (GPS, G + C, and G + C + R). The bottom two rows are the single-frequency RTK/INS integration (GPS, G + C, and G + C + R). The correctly-fixed solutions are shown in green, incorrectly-fixed solutions in red, and float solutions in grey. A zoom-in window is provided to show the details of the correctly fixed solutions in the horizontal (north, east) and vertical (down) time-series. Note the different scale for the tightly-coupled RTK/INS integration.

For the high-accuracy positioning in urban environments, the measurements are easily affected by multipath outliers, especially for those from low-elevation satellites. These measurement outliers will make reliable AR impossible and bias the final positioning result. With the greatly increased observations from multi-GNSS, the high-accuracy positioning with higher cut-off elevation angles becomes possible. Therefore, we also investigate the positioning capabilities of the combined GPS, BeiDou, and GLONASS systems with elevation cut-off angles of 25°, 30°, and 35°.

Figure 11 shows the time series of the position differences in the north, east, and vertical directions for single-frequency RTK (1st column), dual-frequency RTK (2nd column), and single-frequency RTK/INS integration (3rd column), respectively. The first two rows are for a 25° cut-off elevation, while the middle two rows and last two rows are for elevation cut-off angles of 30° and 35°, respectively.

The results from Figure 11 indicates that the AR and positioning performance of dual-frequency GPS/BDS/GLONASS RTK are much better than that of the corresponding single-frequency RTK, especially under the higher cut-off elevation angle. Meanwhile, the performance of the dual-frequency multi-GNSS RTK does not degrade obviously with the increasing cut-off elevation angles, while this is not the case for the single-frequency multi-GNSS RTK. In comparison with dual-frequency multi-GNSS RTK, the performance of the tightly-coupled single-frequency multi-GNSS RTK/INS integration is improved further with fewer ambiguity-float solutions and a smaller positioning error. Generally, the quality of the measurements from high-elevation satellites are better than that from low-elevation satellites. However, the position error of ambiguity-float RTK can also be very large with high elevation cut-off angles.

Table 3 shows the corresponding AR and positioning performance of the combined GPS, BDS, and GLONASS system with elevation cut-off angles of 25°, 30°, and 35°. It includes the fixing rate and RMSs of positioning differences of the float and correctly-fixed single-epoch solution.

It can be seen from Table 3 that the fixing rate of single-frequency GPS + BDS + GLONASS RTK is 36.1% with a 25° cut-off elevation angle, and it drops to 20.3% with a 30° cut-off elevation angle and to only 14.7% with a 35° cut-off elevation angle. By comparison, the dual-frequency GPS + BDS + GLONASS RTK achieves much higher AR fixing rates of 77.7%, 74.3%, and 71.5% for cut-off elevation angles of 25°, 30°, and 35°, respectively. For the tightly-coupled single-frequency GPS + BDS + GLONASS RTK/INS integration, further improvements of 8.5%, 10.3%, and 10.7% can be obtained with cut-off elevation angles of 25°, 30°, and 35°, respectively.

The results in Table 3 also indicate that centimeter-level poisoning accuracy is available once the ambiguities are correctly fixed. The RMSs of position differences of the correctly-fixed solutions with three different cut-off elevation angles are all within 3 cm in the north-east-down components. The RMSs of the ambiguity-float solutions of the tightly-coupled RTK/INS integration are all within 1 m in the north, east, and vertical directions. By contrast, the RMSs of the corresponding ambiguity-float RTK solutions can reach more than 2 m in the vertical direction.

Table 3. RMSs of positioning difference (north, east, down) of the float and correctly-fixed single-epoch solution and fixing rate P_{FR}(%) of the GPS + BDS + GLONASS system with higher cut-off elevation angles.

Cut-off (°)	**25**				**30**				**35**			
RMS (cm)	**N**	**E**	**D**	**FR**	**N**	**E**	**D**	**FR**	**N**	**E**	**D**	**FR**
L1 RTK	0.35	0.44	1.33	36.1	0.41	0.52	1.95	20.3	0.46	0.54	2.07	14.7
Fixed/Float	78.44	88.31	206.3		81.30	87.39	223.9		81.14	87.75	226.4	
L1 + L2 RTK	0.50	0.56	1.56	77.7	0.60	0.73	2.28	74.3	0.55	0.76	2.60	71.5
Fixed/Float	82.56	100.9	183.5		102.8	102.5	221.2		107.9	103.4	230.4	
L1 + INS	0.54	0.62	1.75	86.2	0.76	0.78	2.51	84.7	0.78	0.77	2.37	82.2
Fixed/Float	20.35	32.28	43.03		35.47	50.04	67.94		36.00	47.65	67.59	

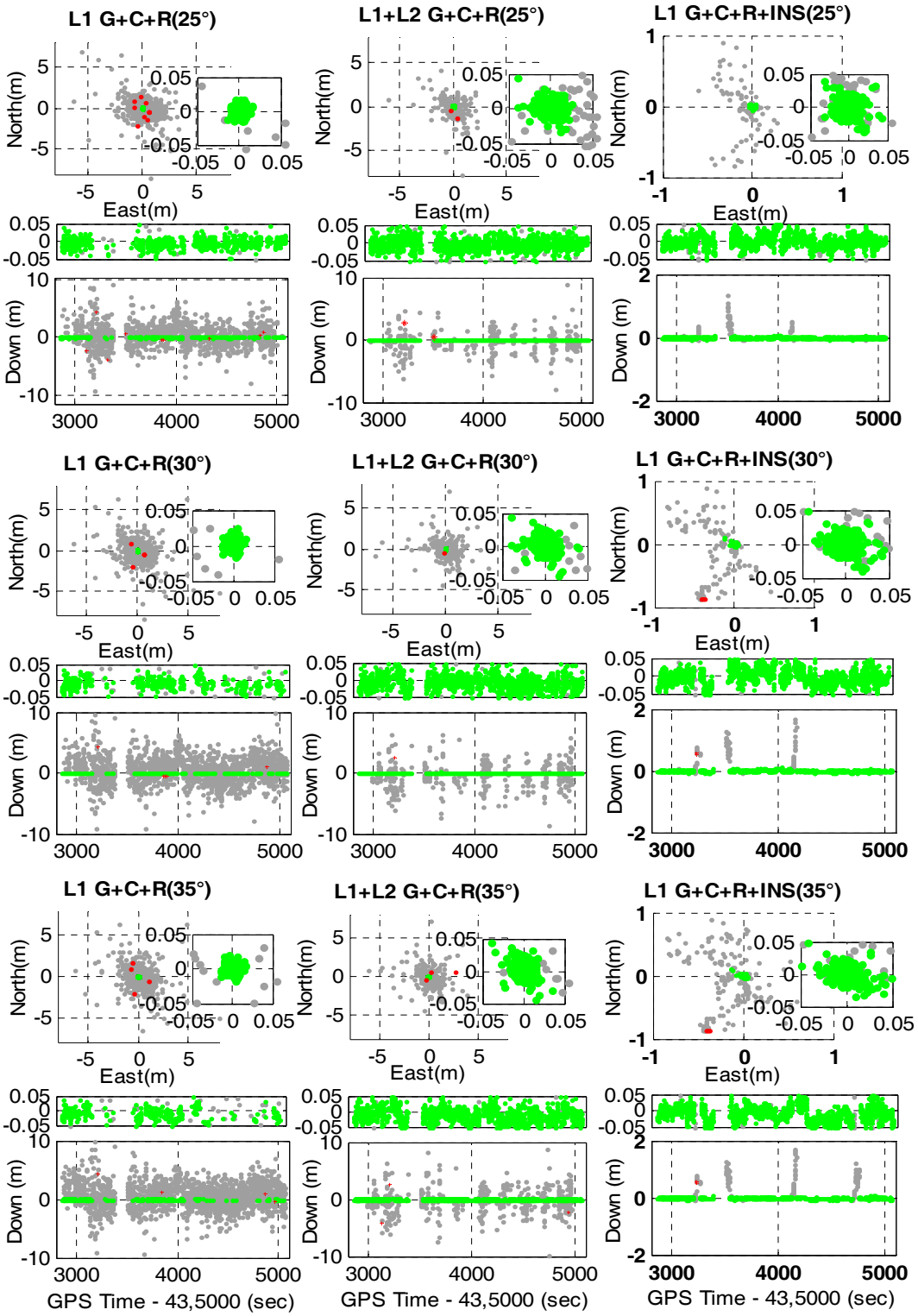

Figure 11. Time series of position differences in the north, east, and vertical directions for single-frequency RTK (G + C + R, 1st column), dual-frequency RTK (G + C + R, 2nd column), and single-frequency RTK/INS integration (G + C + R, 3rd column) with higher cut-off elevation angles (25°, 30°, and 35°). The correctly-fixed solutions are shown in green, incorrectly-fixed solutions in red, and float solutions in grey. A zoom-in window is given to show the details of the correctly-fixed solutions in the horizontal (north, east) and vertical (down) time-series. Note the different scale for the tightly-coupled RTK/INS integration.

4.4. Position Drift Error for Multi-GNSS RTK/INS Integration after the End of GNSS Outages

For most dynamic applications, it is inevitable for vehicles to go through the overpasses, trees and tunnels, etc. In these conditions, the satellite signals may lose lock frequently no matter the single GPS or the multi-GNSS is used. The frequent signal loss makes the GNSS data processing more complicated, especially for the carrier-phase based high-accuracy positioning. Figure 12 shows the GNSS outage (it cannot provide RTK solutions) durations during the driving test for the combined GPS, BDS, and GLONASS system with a 15° cut-off elevation angle. Three zoom-in windows are given to show the magnitude of the outage duration wherein the longest outage lasts more than 2 min and some others are within 10 s.

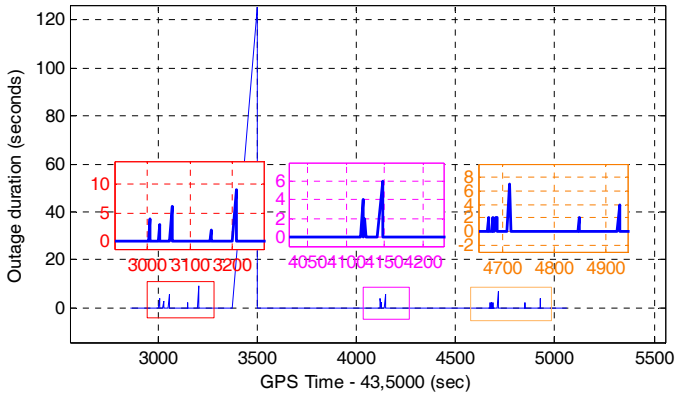

Figure 12. GNSS outage durations during the driving test for the combined GPS, BDS, and GLONASS system with a 15° cut-off elevation angle.

Since the high-precision position information during the long outages is not available in the real experiments, the maximum position error is used to evaluate the positioning performance in the data analysis. Generally, the position errors reach the maximum at the end of outages and the accurate reference position at this epoch can be obtained by applying backward smoothing. Table 4 shows all the outage durations and the corresponding maximum position drift errors.

Table 4. The GNSS outage durations in the field test and the corresponding maximum position drift errors.

Outage Items		**#1**	**#2**	**#3**	**#4**	**#5**	**#6**	**#7**	**#8**	**#9**	**#10**	**#11**	**#12**	**#13**
Duration (s)		4	3	6	2	9	127	4	6	2	2	7	2	4
MAX (cm)	North	0.4	1.2	5.6	1.9	0.9	523.5	1.9	5.8	7.1	6.8	6.7	1.5	3.2
	East	6.2	0.4	9.3	1.7	15.3	1739.3	1.1	14.6	1.5	0.3	14.7	4.2	3.2
	Down	7.1	1.6	5.5	1.4	4.8	2817.3	6.9	1.1	2.3	8.7	1.4	1.4	1.7
	3D	9.4	2.0	12.2	2.9	16.1	3352.1	7.2	15.7	7.6	11.0	16.2	4.7	4.8

It can be seen from Table 4 that the maximum drift at the longest outage duration is up to 5.235, 17.393, and 33.521 m in the north, east, and vertical components. It is also clear that the position drift becomes larger when the outage duration increases. It is mainly due to the uncompensated IMU errors and these errors will lead to the rapid growth of position drift for MEMS inertial sensors. Generally, centimeter-level positioning accuracy can be obtained when the outage duration is within 4 s for the POS1100 MEMS grade IMU. This capability to provide high-accuracy navigation results within short-term outages is meaningful for some navigation applications.

5. Conclusions

Carrier-phase-based high-accuracy positioning in urban environments is still a challenging task, even using high-cost dual-frequency receivers. In this contribution, the tightly-coupled integration of

the single-frequency multi-GNSS RTK and low-cost MEMS-IMU was developed to provide reliable and continuous high-accuracy positioning in GNSS-challenged environments. The outlier-resistant AR and Kalman filtering strategy was proposed specifically for the integration algorithm to resist the measurement outliers. A field vehicular test was carried out to investigate the high-accuracy positioning capabilities of the proposed algorithm in urban environments. Comparisons in terms of AR and positioning performance have been conducted with respect to the single- and dual-frequency multi-GNSS RTK. The following conclusions can be drawn based on the presented results and analysis in this research.

In urban environments, the satellite tracking condition is poor due to the frequent loss-of-lock of the satellite signal, and the degraded satellite availability poses serious challenges to positioning, especially for the single GPS system. The GNSS observations are susceptible to outliers in such environments. Therefore, the fault detection and exclusion is definitely required for reliable positioning; otherwise, the reliable ambiguity resolution is impossible when measurement outliers are in the GNSS data. The proposed outlier-resistant ambiguity resolution and Kalman filtering strategy are suitable for the tightly-coupled integration algorithm and effective to improve the ambiguity resolution performance. By applying an outlier-resistant ambiguity resolution and filtering strategy, the ambiguity-fixed solutions can be obtained even though the measurements are contaminated with large outliers.

The AR and positioning performance of GPS is very poor in urban environments, even using the dual-frequency RTK. As expected, the multi-GNSS can greatly improve the positioning performance due to the increased satellite availability and better spatial geometry structure. The fixing rate of single-frequency GPS RTK increases from 0.1% to 25.1% and 44.7% of the GPS/BDS and GPS/BDS/GLONASS RTK, respectively. The dual-frequency RTK can obtain much better results than the corresponding single-frequency RTK with fixing rates of 10.4%, 75.8%, and 76.7% for the GPS, GPS/BDS, and GPS/BDS/GLONASS, respectively. The performance can be further improved by the single-frequency multi-GNSS RTK/MEMS-IMU tightly-coupled integration with fewer ambiguity-float solutions and smaller positioning error than the corresponding dual-frequency multi-GNSS RTK. The corresponding fixing rate for the GPS, GPS/BDS, and GPS/BDS/GLONASS are 5.8%, 86.1%, and 86.1%, respectively. Additionally, the position errors of ambiguity-float RTK are large even with a higher cut-off elevation angle because it mainly relies on the relatively imprecise code measurements. By contrast, the ambiguity-float solution of the RTK/INS tightly-coupled integration is more stable and accurate due to the strong constraint from the INS in the short-term period.

The results also show that high-accuracy positioning is feasible with limited performance loss for the single-frequency GPS/BDS/GLONASS/INS integration when higher cut-off elevation angles are applied in urban environments. Its AR fixing rate is 86.2%, 84.7%, and 82.2% when the cut-off elevation angles are set to 25°, 30°, and 35°, respectively. Compared with the high-cost dual-frequency RTK, the tightly-coupled integration of single-frequency multi-GNSS and low-cost MEMS-IMU are promising and preferred for some applications in urban environments.

For long outage durations, it is difficult to obtain centimeter-level positioning accuracy during the GNSS outage. Therefore, other aiding sensors and methods will be considered in the future to further improve the high-accuracy positioning capabilities. In addition, suitable methods should be developed to model the multipath error on the carrier phase.

Acknowledgments: We would like to thank the anonymous reviewers for their valuable comments and critical remarks, which greatly improved the quality of the manuscript. This work is supported in part by the National Key Research and Development Program of China (nos. 2016YFB0501800, 2016YFB0501803 and 2016YFB0501804), in part by the National High Technology Research and Develop Program of China (no. 2015AA124002) and, in part, by the National Natural Science Foundations of China (no. 41404029).

Author Contributions: Tuan Li and Hongping Zhang conceived the initial idea; Tuan Li designed the experiment and implemented the software for this contribution; Tuan Li analyzed the data and wrote the main manuscript; Zhouzheng Gao and Qijin Chen helped with the data analysis; and Hongping Zhang and Xiaoji Niu helped with the writing. All authors reviewed the manuscript.

Conflicts of Interest: The authors declare no conflict of interest.

References

1. He, H.; Li, J.; Yang, Y.; Xu, J.; Guo, H.; Wang, A. Performance assessment of single- and dual-frequency BeiDou/GPS single-epoch kinematic positioning. *GPS Solut.* **2014**, *18*, 393–403. [CrossRef]
2. Ong, R.B.; Petovello, M.G.; Lachapelle, G. Assessment of GPS/GLONASS RTK under Various Operational Conditions. In Proceedings of the 22nd International Technical Meeting of The Satellite Division of the Institute of Navigation (ION GNSS 2009), Savannah, GA, USA, 22–25 September 2009; pp. 3297–3308.
3. Carcanague, S.; Julien, O.; Vigneau, W.; Macabiau, C. Low-Cost Single-Frequency GPS/GLONASS RTK for Road Users. In Proceedings of the ION 2013 Pacific PNT Meeting, Honolulu, HI, USA, 23–25 April 2013; pp. 168–184.
4. Montenbruck, O.; Steigenberger, P.; Khachikyan, R.; Weber, G.; Langley, R.B.; Mervart, L.; Hugentobler, U. IGS-MGEX: Preparing the ground for multi-constellation GNSS science. *Inside GNSS* **2014**, *9*, 42–49.
5. Teunissen, P.J.G.; Odolinski, R.; Odijk, D. Instantaneous BeiDou+GPS RTK positioning with high cut-off elevation angles. *J. Geod.* **2013**, *88*, 335–350. [CrossRef]
6. Odolinski, R.; Teunissen, P.J.G. Low-cost, high-precision, single-frequency GPS–BDS RTK positioning. *GPS Solut.* **2017**, *21*, 1315–1330. [CrossRef]
7. Li, T.; Zhang, H.; Niu, X.; Gao, Z. Tightly-Coupled Integration of Multi-GNSS Single-Frequency RTK and MEMS-IMU for Enhanced Positioning Performance. *Sensors* **2017**, *17*, 2462. [CrossRef] [PubMed]
8. Odolinski, R.; Teunissen, P.J.G.; Odijk, D. Combined BDS, Galileo, QZSS and GPS single-frequency RTK. *GPS Solut.* **2014**, *19*, 151–163. [CrossRef]
9. Wanninger, L.; Wallstab-Freitag, S. Combined Processing of GPS, GLONASS, and SBAS Code Phase and Carrier Phase Measurements. In Proceedings of the 20th International Technical Meeting of the Satellite Division of The Institute of Navigation (ION GNSS 2007), Fort Worth, TX, USA, 25–28 September 2007; pp. 866–875.
10. Sleewaegen, J.; Simsky, A.; De Wilde, W.; Boon, F.; Willems, T. Demystifying GLONASS inter-frequency carrier phase bias. *Inside GNSS* **2012**, *7*, 57–61.
11. Wanninger, L. Carrier-phase inter-frequency biases of GLONASS receivers. *J. Geod.* **2012**, *86*, 139–148. [CrossRef]
12. Tian, Y.; Ge, M.; Neitzel, F. Particle filter-based estimation of inter-frequency phase bias for real-time GLONASS integer ambiguity resolution. *J. Geod.* **2015**, *89*, 1145–1158. [CrossRef]
13. Gao, Z.; Shen, W.; Zhang, H.; Ge, M.; Niu, X. Application of Helmert Variance Component Based Adaptive Kalman Filter in Multi-GNSS PPP/INS Tightly Coupled Integration. *Remote Sens.* **2016**, *8*, 553. [CrossRef]
14. Grejner-Brzezinska, D.A.; Da, R.; Toth, C. GPS error modeling and OTF ambiguity resolution for high-accuracy GPS/INS integrated system. *J. Geod.* **1998**, *72*, 626–638. [CrossRef]
15. Niu, X.; Zhang, Q.; Gong, L.; Liu, C.; Zhang, H.; Shi, C.; Wang, J.; Coleman, M. Development and evaluation of GNSS/INS data processing software for position and orientation systems. *Surv. Rev.* **2015**, *47*, 87–98. [CrossRef]
16. Falco, G.; Einicke, G.A.; Malos, J.T.; Dovis, F. Performance Analysis of Constrained Loosely Coupled GPS/INS Integration Solutions. *Sensors* **2012**, *12*, 15983–16007. [CrossRef] [PubMed]
17. Jiang, S.; Jiang, W. On-Board GNSS/IMU Assisted Feature Extraction and Matching for Oblique UAV Images. *Remote Sens.* **2017**, *9*, 813. [CrossRef]
18. Hide, C.; Moore, T. GPS and Low Cost INS Integration for Positioning in the Urban Environment. In Proceedings of the 18th International Technical Meeting of the Satellite Division of the Institute of Navigation, Long Beach, CA, USA, 13–16 September 2005; pp. 1007–1015.
19. Godha, S.; Cannon, M.E. GPS/MEMS INS integrated system for navigation in urban areas. *GPS Solut.* **2007**, *11*, 193–203. [CrossRef]
20. Chiang, K.-W.; Duong, T.; Liao, J.-K. The Performance Analysis of a Real-Time Integrated INS/GPS Vehicle Navigation System with Abnormal GPS Measurement Elimination. *Sensors* **2013**, *13*, 10599–10622. [CrossRef] [PubMed]

21. Falco, G.; Gutiérrez, C.C.; Serna, E.P.; Zacchello, F.; Bories, S. Low-cost Real-time Tightly-Coupled GNSS/INS Navigation System Based on Carrier-phase Double- differences for UAV Applications. In Proceedings of the 27th International Technical Meeting of the Satellite Division of The Institute of Navigation (ION GNSS 2014), Tampa, FL, USA, 8–12 September 2014; pp. 841–857.
22. Eling, C.; Klingbeil, L.; Kuhlmann, H. Real-Time Single-Frequency GPS/MEMS-IMU Attitude Determination of Lightweight UAVs. *Sensors* **2015**, *15*, 26212–26235. [CrossRef] [PubMed]
23. Zhao, S.; Chen, Y.; Farrell, J.A. High-Precision Vehicle Navigation in Urban Environments Using an MEM's IMU and Single-Frequency GPS Receiver. *IEEE Trans. Intell. Transp. Syst.* **2016**, *17*, 2854–2867. [CrossRef]
24. Falco, G.; Pini, M.; Marucco, G. Loose and Tight GNSS/INS Integrations: Comparison of Performance Assessed in Real Urban Scenarios. *Sensors* **2017**, *17*, 255. [CrossRef] [PubMed]
25. Dorn, M.; Filwarny, J.O.; Wieser, M. Inertially-aided RTK based on tightly-coupled integration using low-cost GNSS receivers. In Proceedings of the 2017 European Navigation Conference (ENC), Lausanne, Switzerland, 9–12 May 2017; pp. 186–197.
26. Teunissen, P.J.G. Quality control in integrated navigation systems. In Proceedings of the IEEE Symposium on Position Location and Navigation. A Decade of Excellence in the Navigation Sciences, Las Vegas, NV, USA, 20–23 March 1990; pp. 158–165.
27. Gillissen, I.; Elema, I.A. Test results of DIA: A real-time adaptive integrity monitoring procedure, used in an integrated navigation system. *Int. Hydrogr. Rev.* **1996**, *73*, 75–100.
28. Clark, B.J.; Bevly, D.M. GPS/INS integration with fault detection and exclusion in shadowed environments. In Proceedings of the IEEE/ION Position, Location and Navigation Symposium, Monterey, CA, USA, 5–8 May 2008; pp. 1–8.
29. Hewitson, S.; Wang, J. Extended receiver autonomous integrity monitoring (eRAIM) for GNSS/INS integration. *J. Surv. Eng.* **2007**, *136*, 13–22. [CrossRef]
30. Benson, D.O. A Comparison of Two Approaches to Pure-Inertial and Doppler-Inertial Error Analysis. *IEEE Trans. Aerosp. Electron. Syst.* **1975**, *4*, 447–455. [CrossRef]
31. Park, M. Error Analysis and Stochastic Modeling of MEMS Based Inertial Sensors for Land Vehicle Navigation Applications. Ph.D. Thesis, University of Calgary, Calgary, AB, Canada, April 2004.
32. Petovello, M. GLONASS inter-frequency biases and ambiguity resolution. *Inside GNSS* **2009**, *4*, 24–28.
33. Gendt, G.; Dick, G.; Reigber, C.H.; Tomassini, M.; Liu, Y.; Ramatschi, M. Demonstration of NRT GPS Water Vapor Monitoring for Numerical Weather Prediction in Germany. *J. Meteorol. Soc. Jpn.* **2003**, *82*, 360–370.
34. Shin, E.-H. Estimation Techniques for Low-Cost Inertial Navigation. Ph.D. Thesis, The University of Calgary, Calgary, AB, Canada, May 2005.
35. Scherzinger, B.M. Robust Positioning with Single Frequency Inertially Aided RTK. In Proceedings of the 2002 National Technical Meeting of the Institute of Navigation, San Diego, CA, USA, 28–30 January 2002; pp. 911–917.
36. Teunissen, P.J.G. The Least-Squares Ambiguity Decorrelation Adjustment: A Method for Fast GPS Integer Ambiguity Estimation. *J. Geod.* **1995**, *70*, 65–82. [CrossRef]
37. Ji, S.; Chen, W.; Ding, X.; Chen, Y.; Zhao, C.; Hu, C. Ambiguity validation with combined ratio test and ellipsoidal integer aperture estimator. *J. Geod.* **2010**, *84*, 597–604. [CrossRef]
38. Verhagen, S. On the Reliability of Integer Ambiguity Resolution. *Navigation* **2005**, *52*, 99–110. [CrossRef]
39. Yang, Y.; Song, L.; Xu, T. Robust estimator for correlated observations based on bifactor equivalent weights. *J. Geod.* **2002**, *76*, 353–358. [CrossRef]
40. Savage, P.G. Strapdown inertial navigation integration algorithm design part 1: Attitude algorithms. *J. Guid. Control Dyn.* **1998**, *21*, 19–28. [CrossRef]
41. Savage, P.G. Strapdown inertial navigation integration algorithm design part 2: Velocity and position algorithms. *J. Guid. Control Dyn.* **1998**, *21*, 208–221. [CrossRef]
42. Deng, C.; Tang, W.; Liu, J.; Shi, C. Reliable single-epoch ambiguity resolution for short baselines using combined GPS/BeiDou system. *GPS Solut.* **2013**, *18*, 375–386. [CrossRef]
43. Gelb, A. *Applied Optimal Estimation*; MIT Press: Cambridge, MA, USA, 1974; pp. 160–165.

© 2018 by the authors. Licensee MDPI, Basel, Switzerland. This article is an open access article distributed under the terms and conditions of the Creative Commons Attribution (CC BY) license (http://creativecommons.org/licenses/by/4.0/).